*Materials Science Forum Vol.682 (2011) pp 123-130*
*© (2011) Trans Tech Publications, Switzerland*
*doi:10.4028/www.scientific.net/MSF.682.123*

# Mechanical Property of Duplex Stainless Steel with Nanostructured Layer by Surface Mechanical Attrition Treatment

L. Chen[1, a], X.L. Wu[1, b]

[1]State Key Laboratory of Nonlinear Mechanics, Institute of Mechanics, Chinese Academy of Science, Beijing 100190, China

[a]chenliu@imech.ac.cn, [b]xlwu@imech.ac.cn,

**Keywords:** nanostructure, mechanical property, surface mechanical attrition treatment, duplex stainless steel

**Abstract.** A grain size gradient layer material was produced by means of surface mechanical attrition treatment on a UNS S32304 duplex stainless steel. In this study, the mechanical property was characterized by tensile test, while microstructure was investigated by transmission electron microscopy, scanning electron microscopy and electron backscatter diffraction. The deformed layer enhanced both the yield strength and maximum strength with large ductility retained, as revealed by tensile test that the yield stress of 30 minutes processed sample was 702 MPa as compared with 454 MPa of as-annealed sample. The elongation to failure, however, decreased from 0.41 to 0.27.

## Introduction

Nanostructured materials usually possess high strength due to their small grain size, but the limited ductility as a dark cloud always appears on the horizon of material scientists. Therefore, intensive researches with different microstructural designs have been sparked to improve the ductility of nanostructured materials during past decades [1-6].

During those structural designs, gradient layered materials produced by severe surface plastic deformation exhibit good optimizations of tensile strength and elongation to failure, such as low carbon steel plate of 1.5 mm thick treated by high-energy shot peening (HESP) [7], 316 stainless steel treated by surface mechanical attrition treatment (SMAT) [8], nickel-base alloy subjected to surface nanocrystallization and hardening (SNH) [9] and introducing non-localized fracture behavior by co-rolling the SMATed AISI 304 stainless steel [10].

In this work, a duplex stainless steel UNS S32304 subjected to surface mechanical attrition treatment was investigated. The research contents contain tensile property, microstructure characterization and fracture surfaces analysis.

## Experimental Methods

The DSS used in this investigation is a commercially stainless steel sheet. The as-rolled sheet was 1.5 mm thick. A heat treatment (1100 $^{\circ}$C for 60 min, followed by oil quenching) was performed so as to obtain a dual phase microstructure. After annealing, the plates were surface polished with silicon carbide paper to grade 1500.

The SMAT techniques have been used to introduce gradient layer. The details about SMAT processing were reported elsewhere [6,11]. In this work, the hard balls with 4 mm in diameter and 20 kHz on frequency were used to provide high density peening for 30 minutes on both surfaces.

The plates were then cut into dog-bone shape tensile specimen with a rectangular cross-section (2.5mm×1.5mm) and a gauge length 14.5mm by electrical discharging. Tensile tests were conducted on an Instron 5565 test machine with a video extensometer which has accuracy more than 0.5%, and the moving speed of crossbeam was controlled at 0.2mm per minutes.

Samples were prepared for optic microscopy by grinding and then polishing. A special electrolytic etching technique with 40pct vol. $HNO_3$ aqueous solution (1.1V, 40s) followed by Murakami's solution (30g $K_3Fe(CN)_6$, 10g KOH and 100ml $H_2O$) [12]. TEM thin foils were prepared by jet polishing with a solution of 95% ethyl alcohol and 5% perchloric acid ($HClO_4$) at -20°C, applying a voltage of 20V.

The fracture of tensile specimens was investigated by scanning electron microscope (HITACHI S-570), and the microstructure was characterized by transmission electron microscope (JEM 200CX).

## Results and Discussion

**Mechanical Properties.** Fig. 1 shows the tensile stress-strain curves of UNS S32304 specimens, and Table 1 lists the specific property parameters in detail. Specifically, the 0.2% offset yield strength and ultimate tensile strength have increased by ~55% and ~10% after 30min treatment, respectively. However, the uniform elongation and the elongation to failure have been decreased from 30% and 41% to 14% and 27% respectively. The reduction of area has decreased by 10% after 30min treatment. Additionally, the value of UTS/$\sigma_Y$ has decreased from 1.58 to 1.12.

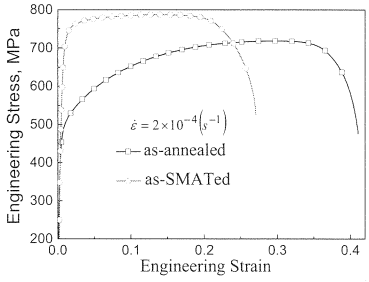


Fig. 1. Engineering stress-strain curves for as-annealed and SMATed samples.

Table 1. Summary of tensile properties of as-annealed and SMATed samples. Yield stress $\sigma_Y$, ultimate tensile strength UTS, uniform elongation $\varepsilon_U$, elongation to failure $\varepsilon_{total}$, and the reduction of area $\Psi$.

| Specimen | $\sigma_Y$ (MPa) | UTS (MPa) | $\varepsilon_U$ (%) | $\varepsilon_{total}$ (%) | ($\Psi$) (%) | UTS/$\sigma_Y$ |
|---|---|---|---|---|---|---|
| as-annealed | 454 | 719 | 29.62 | 41.06 | 76.23 | 1.58 |
| as-SMATed | 702 | 787 | 14.02 | 27.04 | 68.67 | 1.12 |

Fig. 2 shows the work hardening rate ($\Theta$) plotted versus true strain and true stress, respectively. As seen in Fig. 2(a), the work hardening rate of SMATed sample is remarkably lower than as-annealed sample over a range of strain. Additionally, both samples exhibit a steep decrease

with increasing strain or stress reflecting elastoplastic transition beyond the yield point and before reaching a plateau which defined as hardening stage II [13].

In order to further quantify the work hardening response, the Ludwik formula (Eq. 1) was used to fit the uniform stage in tensile curve. The results are shown in Table 2.

$$\sigma = k_1 + k_2 \varepsilon^n \tag{1}$$

where σ and ε represent true stress and plastic strain respectively. n is the work hardening coefficient and K1 is the initial yield stress, which is especially important for materials with high yield stress. K2 represents the increment of strength due to work hardening with ε = 1. The surface treatment lead n value decrease from 0.54 to 0.29, which in line with the decrease of tensile ductility.

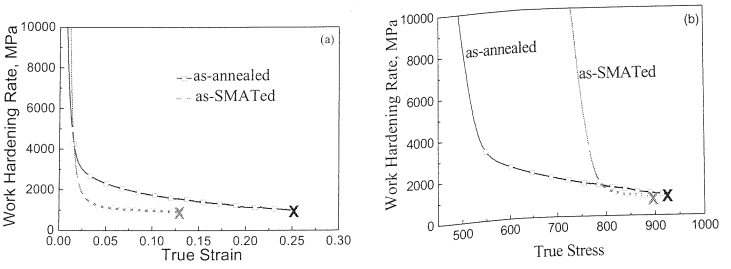


Fig. 2. Work hardening rate (calculated by $\Theta = \left(\frac{\partial \sigma}{\partial \varepsilon}\right)_{\dot{\varepsilon}}$) plotted vs. (a) true strain and (b) true stress.

Table 2. Work hardening parameters calculated by fitting the uniaxial tensile stress-strain curves with eq. (1) for SMATed sample.

| Specimen | $K_1$ (MPa) | $K_2$ (MPa) | $n$ |
|---|---|---|---|
| as-annealed | 454 | 1065 ± 8.3E-5 | 0.54 ± 2.6E-4 |
| as-SMATed | 702 | 498 ± 2.7E-4 | 0.29 ± 6.0E-4 |

**Microstructure Characterization.** Fig. 3 shows the cross-sectional microstructure of the as-annealed and as-SMATed samples. The as-annealed sample has two conspicuous features as depicted in Fig. 3(a). First, near-lamellar microstructure is visible. The light phase is austenite and the contrast is ferrite. The grain boundaries in both γ and α phase are clear, but the annealed twin boundaries in γ phase are invisible because it's difficult to obtain the contrast of this two phases and details such as boundaries in each phase simultaneously by optic microscopy technique. Second, the lamellar γ phase is surrounded by α matrix. Fig. 3(b) shows the severe deformed layer has been formed where phase boundaries are not straight any more.

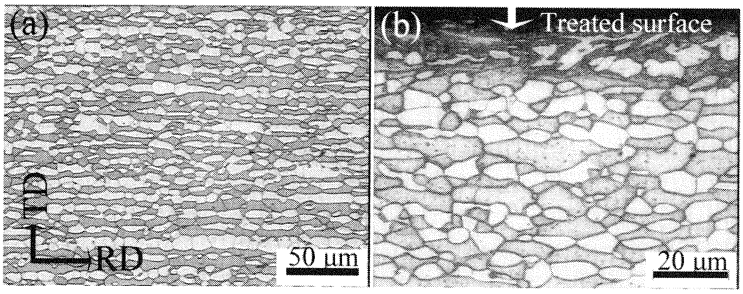


Fig. 3. Optical microscopic images of the: (a) as-received and (b) 30 minutes SMA-treated samples.

Fig. 4 shows the distributions of misorientation angles determined by EBSD. Fig. 4(a), (b) and (c) show the distribution of misorientation angles in γ phase at different deep (50, 140 and 200 μm, respectively). The low angle grain boundaries (LAGBs) are increasing with the decrease of depth far from the treated surface. The peaks at the lowest angle of 2° (the angle below 2° is not calculated due to the angle resolution) is 2.6%, 8.8% and 10.3% at the depth of 200μm, 140μm and 50μm, respectively. Additionally, the peak at the angle of 50.8° is due to Σ3 coincident-site lattice twin boundaries.

Fig. 4(d), (e) and (f) depict the distribution of misorientation angles in α phase at the same area with Fig. 4(a), (b) and (c). The LAGBs are increasing with the decreasing of depth too. The lowest angle of 2° is 6.4%, 12.2% and 10.5% at the depth of 200μm, 140μm and 50μm. Note the fraction of 2° misorientation angle boundaries at 50μm is lower than the value at the deep of 140 μm, it's the result of increases of other LAGBs (e.g. the fraction of 8° misorientation angle boundaries is 4.3% at the depth of 50 μm compared with 1.5% at the 140 μm deep).

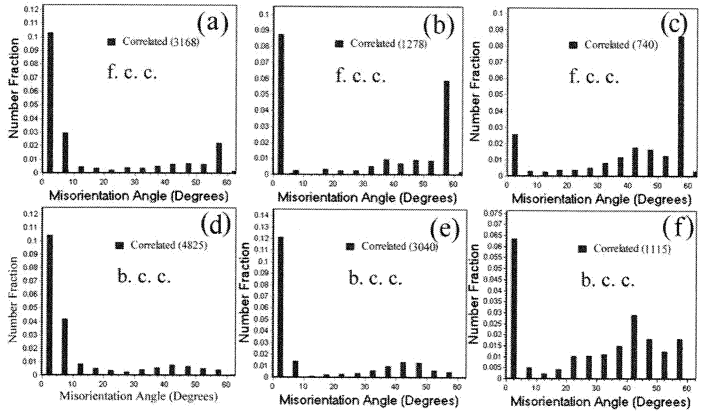


Fig. 4. Distributions of boundary misorientation angles in γ phase (f. c. c.) and α phase (b. c.c.) at the depth of (a and d) 50 μm, (b and e) 140 μm, (c and f) 200 μm far from the treated surface, respectively. The observed plane is RD×ND, and all maps are calculated from a rectangular area with 100×70 μm. The depth is defined by the length from the centre of each selected area to the treated surface.

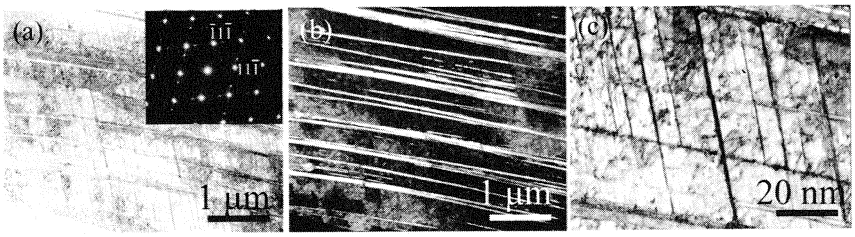


Fig. 5. TEM images displaying the typical microstructure (~30 μm deep) of SMATed sample. (a) Bright-field image of deformation twin in γ phase; (b) dark-field image of twin; (c) microtwin at high magnification.

Fig. 5 shows a typical microstructure observed at about 30 μm from the treated surface. Fig. 5(a) displays two sets of deformation twins. The direction of incident electron beam is <011> which calculated from the inset SAED pattern in Fig. 5(a). The diffraction pattern evidently demonstrate that two sets of twins are symmetrical with $\{11\bar{1}\}$ and $\{\bar{1}1\bar{1}\}$ plane, respectively. Fig. 5(b) is a dark-field image of twin. Fig. 5(c) shows the microtwins at high magnification in which divide the matrix γ phase into rhombic blocks by twin-twin intersection.

The twin boundary is a particularly case with high angle misorientation. So, deformed grains are subdivided by mechanical twin in some metals or alloys with low stacking faults, i.e., twin-twin intersection in AISI 304 stainless [14]. In this paper, only the microstructure at the deep of 30 μm was investigated. The intersection of twins would be connected to the underlying grain refinement mechanism in γ phase.

**Fracture Mechanism.** Fig. 6(a) and (b) show a representative example of fracture geometry of the as-annealed sample from the direction of width (W) and thickness (T), respectively. Fig. 6(c) and (d) are the profiles of SMATed specimen from the W and T direction, where some microcracks were identified by white arrows on the top plane of gauge section. The angles between the failure plane and the loading axis are 66° and 55° for as-annealed and SMATed samples, respectively.

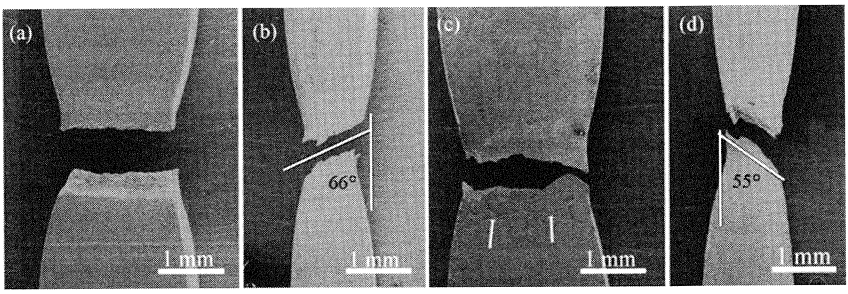


Fig. 6. SEM images displaying the fracture geometry of (a and b) as-received and (c and d) 30 min treated sample from the direction of width (W) and thickness (T), respectively.

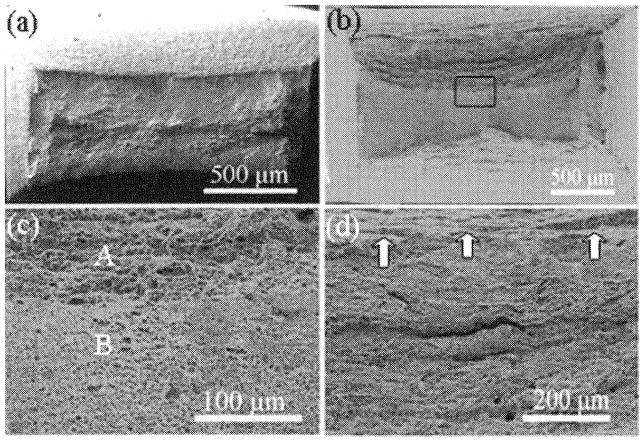


Fig. 7. SEM images of fracture surfaces. (a) Fracture surface of as-annealed sample; (b) fracture surface of SMATed sample showing two types of morphologies; (c) magnified region from selected area, which showing the size of dimples on the upper side (marked by letter A) is lager than the other side (marked by letter B); (d) microcracks in zone A near the SMA treated surface.

Fig. 7(a) shows the fracture surface of as-annealed sample. Fig. 7(b) shows a fracture surface consisted of two types of morphologies, which are divided by a distinct arc boundary. The difference between Fig. 7(a) and Fig. 7(b) demonstrate clearly that the deformed layers have impacted the fracture mechanism of SMATed specimens of DSS. Fig. 7(c) is the magnified image of square area on Fig. 7(b), which exhibits the difference of dimples size between zone A and zone B. It's true that the dimples size from region A is obvious larger than one from region B. Fig. 7(d) shows the microcracks from zone A. Note the distance between the main crack (larger one) and the SMATed surface is about 200 μm. Additionally, its interesting to note that the growth path of microcracks is parallel to the arc boundary between zone A and zone B through the combination of Fig. 7(b) and (d).

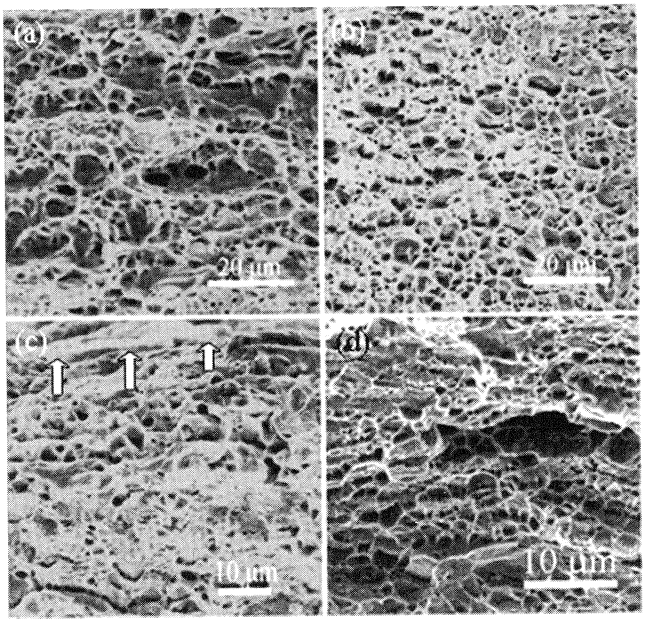


Fig. 8. SEM images displaying the dimples of SMATed sample from (a) zone A and (b) zone B near the boundary between two morphologies, as well as the site near the SMA treated surface which identified by white arrows. The dimples of as-annealed sample on the centre region of fracture surface shown in (d) for contrast.

Fig. 8(a) and (b) show the extensive dimples of SMATed specimen on zone A and B. The dimples from zone A is obvious larger than dimples from zone B. Additionally, the larger dimples in Fig. 8(a) are formed by tearing ridge in α phase in which failured with dimples and quasi-cleavage features. Fig. 8(c) exhibits the morphology under the SMATed surface, which state clearly the exist of dimples on the fracture surface from the severely deformed layer. Fig. 8(d) shows the representative dimples on the center region of fracture surface of as-received specimen.

The fracture surface of SMATed sample consist of microcracks and extensive dimples. Therefore, the coalescence of microvoid and propagations of microcracks must play an important role in the fracture process. The main crack at the deep of ~200 μm illustrates the propagation of microcracks started at the transitional area between the deformed layer and matrix.

Both the as-annealed and SMATed specimen exhibit equiaxed morphologies, its different from the observation in other gradient materials in which elongated dimples exist due to shear stress. Furthermore, the dimples near the SMATed surface in zone A is observed. The dimple size in zone A is obviously larger than dimples in zone B, and one underlying reason is the stress relaxtion due to propagation of microcracks. It can be demonstrated by Fig. 7(b) in which the upper surface in nearly straight while the other surface is bended clearly attributed to the nucleation and propagation of microcracks on one side of the frature surface.

## Summary

A type of duplex stainless steel UNS S32304 with gradient layer was investigated. Optic microscopy exhibits the near-lamellar structure with the thickness about 8 μm was formed in as-annealed materials. The distribution of misorientation angles in SMATed specimens shows the

increase of LAGBs with the decrease of depth far from the treated surface, and the fraction of LAGBs in α phase at the same deep is higher than the value in γ phase. The results of tensile testing, TEM evaluation and detailed fractographic analysis of fracture surface led to the following summaries:

1. The DSS plates with a thickness of 1.5 mm after SMAT for 30 min display reasonable combination of high strength and tensile ductility. The yield strength has improved by 55% and the elongation to failure equals to 29%.
2. The work hardening coefficient of SMATed samples equal to 0.29 as compared with 0.54 of as-annealed specimens.
3. TEM investigation at the deep about 30 μm displays a large amount of twins in γ phase (The intersection of twins divided the matrix into small rhombic blocks).
4. The microcracks propagate at the transitional region between the deformed layer and the matrix.
5. The fracture surfaces of SMATed specimens show two types of morphologies divided by an arc boundary which parallel to the growth path of microcracks. The one is consist of microcracks and larger dimples, and the other one is composed of smaller dimples and all the dimples are equiaxed. Furthermore, the features of quasi-cleavage with tearing ridge are clear.

**References**

[1] K. Lu, L. Lu and S. Suresh: Science Vol. 324 (2009), p. 349

[2] E. Ma: Scr. Mater. Vol. 49 (2003), p. 663

[3] C.C. Koch; Scr. Mater Vol. 49 (2003), p. 657

[4] Y.M. Wang, M.W. Chen, F.Z. Zhou and E. Ma: Nature Vol. 419 (2002), p. 912

[5] Y.H. Zhao, T. Topping, J.F. Bingert, J.J. Thornton, A.M. Dangelewicz, Y. Li, W. Liu, Y.T. Zhu, Y.Z. Zhou and E.J. Lavernia: Adv. Mater. Vol. 20 (2008), p. 3028

[6] K. Lu, J. Lu: Mater. Sci. Eng. A Vol. 375-377 (2004), p.38

[7] G. Liu, S.C. Wang, X.F. Lou, J.Lu and K. Lu: Scr. Mater. Vol. 44 (2001), p. 1791

[8] T. Roland, D. Retraint, K. Lu and J. Lu: Mater. Sci. Eng. A Vol. 445-446 (2007), p. 281

[9] J.W. Tian, K. Dai, J.C. Villegas, L. Shaw, P.K. Liaw, D.L. Klarstrom and A.L. Ortiz: Mater, Sci. Eng. A Vol. 493 (2008), p. 176

[10]A.Y. Chen, D.F. Li, J.B. Zhang, H.W. Song and J. Lu: Scr. Mater. Vol. 59 (2008), p. 579

[11]K. Lu, J. Lu: J. Mater. Sci. Tech. Vol 15 (1999), p. 193

[12]E. Johnson, Y.J. Kim, L.S. Chumbley and B. Gleeson: Scr. Mater. Vol 50 (2004), p. 1351

[13]F.D. Torre, P. Spatig, R. Schaublin and M. Victoria: Acta Mater. Vol 53 (2005), p. 2337

[14]H.W. Zhang, Z.K. He, G. Liu, J. Lu and K. Lu: Acta Mater. Vol 51 (2003), p. 1871